Chinese Chemical Letters 36 (2025) 110232

Contents lists available at ScienceDirect

Chinese Chemical Letters

journal homepage: www.elsevier.com/locate/cclet

Methanol steam mediated corrosion engineering towards high-entropy NiFe layered double hydroxide for ultra-stable oxygen evolution

Jinqiang Gao[a,1], Haifeng Yuan[a,1], Xinjuan Du[b], Feng Dong[a], Yu Zhou[a], Shengnan Na[a], Yanpeng Chen[a], Mingyu Hu[c], Mei Hong[a,*], Shihe Yang[a,*]

[a] Guangdong Provincial Key Laboratory of Nano-Micro Materials Research, School of Advanced Materials, Peking University Shenzhen Graduate School (PKUSZ), Shenzhen 518055, China
[b] School of Chemical Engineering and Technology, Xi'an Jiaotong University, Xi'an 710049, China
[c] Department of Physics, Hong Kong Baptist University, Hong Kong 999077, China

ARTICLE INFO

Article history:
Received 16 April 2024
Revised 9 July 2024
Accepted 10 July 2024
Available online 10 July 2024

Keywords:
High-entropy material
Corrosion engineering
NiFe-LDH
Oxygen evolution reaction
Stability

ABSTRACT

Rational design of viable routes to obtain efficient and stable oxygen evolution reaction (OER) electrocatalysts remains challenging, especially under industrial conditions. Here, we provide a solvent-steam assisted corrosion engineering strategy to directly fabricate high-entropy NiFe-LDH with spatially resolved structural order. Ammonium fluoride in methanol steam enables the formation of nanosheets while Fe^{3+} effectively enhances their adhesion to the semi-sacrificial nickel-iron foam (NFF), thereby conjuring up a NiFe-LDH@NFF catalyst that exhibits remarkable adaptability to robust electrochemical activation yet with excellent stability. Comprehensive measurements reveal the *in-situ* formation of high-valance metal oxyhydroxide and the enhancement of adsorption-desorption process. Under the industrial condition (6 mol/L KOH, 60 °C), the NiFe-LDH@NFF exhibits excellent activity of 50 mA/cm^2 at 1.55 V and high durability of over 120 h at 200 mA/cm^2. We anticipate that the steam assisted strategy could promote the development of efficient non-precious electrocatalysts for hydrogen energy.

Renewable energy sources are contributing increasing amounts of electricity to human society [1]. Hydrogen has long been regarded as a promising candidate for addressing future energy and environmental crisis [2,3]. Researchers put great effort to obtain clean hydrogen production [4,5]. Compared to fossil-fuel-based technologies, electrochemical water splitting shows clear technical and environmental advantages [6]. This route has been explored for decades, but the production of hydrogen is still severely limited by the sluggish kinetics of oxygen evolution reaction (OER) [7,8]. While precious metal catalysts offer significant advantages in terms of performance and stability, the overall cost inevitably limits further application of such materials on a large scale [9]. Developing affordable and efficient OER catalysts is essential for advancing electrochemical water splitting towards industrial applications.

For this purpose, various structural rearrangements of non-noble metals have been demonstrated at the atomic/molecular level [10-12]. Earth abundant NiFe-based materials, especially NiFe layered double hydroxides (LDHs) have gradually been recognized as one of the best electrocatalysts for alkaline OER [13-15]. However, when confronting the actual harsh electrolyte, this promising anode still confronts two major challenges. One is maintaining all active sites effective while keeping the fragile layer structure stable [16]. Chen *et al.* demonstrated that the OER performance decay of NiFe-LDH can be attributed to the slow diffusion of interstitial intermediate proton acceptors (*e.g.*, OH^-) [17]. Lei *et al.* discovered a positive relationship between electrocatalytic performance and symmetry reduction, and ingeniously designed high-entropy single-atom activated carbon catalysts to minimize the local symmetry [18]. Another issue is that the catalyst-support anchoring needs to be secured so as to resist physical shedding during the catalytic process [19]. According to current literatures, the activity of modified NiFe-LDH electrodes is superior to that of commercial precious metal catalysts [20-23]. Therefore, the surging demand for its large application has led to an imminent need to promote its structural stability and bonding to the substrate. Meanwhile, the electrode fabrication procedures need to be simplified, given the scalability requirement for its industrial production.

In this study, we demonstrate a facile one-step construction of high-entropy NiFe LDH electrode for sustainable OER, which can

* Corresponding authors.
E-mail addresses: hongmei@pku.edu.cn (M. Hong), chsyang@pku.edu.cn (S. Yang).
[1] These authors contributed equally to this work.

https://doi.org/10.1016/j.cclet.2024.110232
1001-8417/

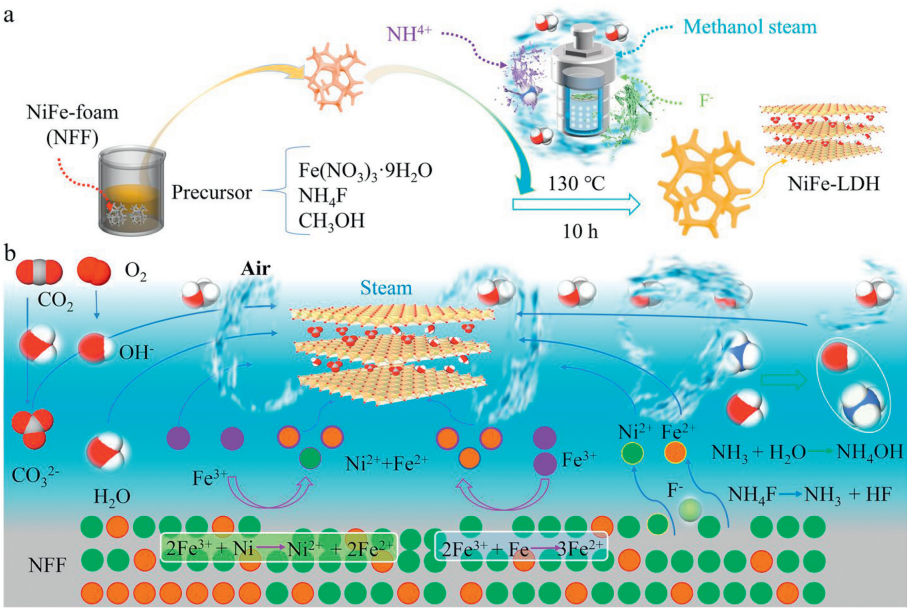

Fig. 1. (a) Schematic illustration of methanol steam mediated corrosion engineering strategy and (b) possible growth mechanism of NiFe-LDH@NFF.

withstand long-time operation under harsh conditions. The synthesis utilized methanol-mediated corrosion engineering of nickel-iron foam (NFF). Fe^{3+} and F^- in MeOH-NH_4F solution efficiently corrode the nickel-iron foam, thus providing the full nickel source (Ni^{2+} ions) and the partial iron source (Fe^{2+} ions) needed to prepare the target NiFe-LDH, which possesses abundant amorphous-crystalline heterointerfaces and juxtaposed single-poly crystalline regions. Under different corrosion conditions and with different supports, the transformation process of the electrode is systematically studied. Compelling evidence indicates that the formation of the chaotic structures, termed high-entropy ones hereafter, helps maintain physical and chemical stability. The continuous cyclic voltammetry (CV) scanning of 100 cycles, termed activation process of NiFe-LDH, effectively promotes the formation of more adaptive structures, leading to the exposure of more active sites. Even under industrial conditions (6 mol/L KOH, 60 °C), the high-entropy NiFe-LDH grown on the semi-sacrificial NFF exhibits high catalytic activity and excellent long-term stability. Thus, this investigation paves a way for the rational design of LDH electrodes with embedded high-entropy structures for efficient and stable electrocatalysis.

The preparation of self-supported NiFe-LDH through a facile methanol steam mediated method is schematically illustrated in Fig. 1a. Here, the NiFe-foam color witnesses a gray-to-yellow transformation (Fig. S1 in Supporting information). As shown in Fig. 2a, uniform nanosheets were *in-situ* grown on NFF by the corrosion engineering strategy, which could transform the semi-sacrificial NFF into Ni and Fe sources [24]. The corrosion transformation is mainly a surface reaction as shown in Fig. 2b and Fig. S2 (Supporting information). The X-ray diffraction (XRD) pattern of NiFe-LDH@NFF only shows three peaks of face-centered cubic bulk NiFe foam structure [25]. To accurately obtain the surface crystal information, the powder was collected for XRD test. The diffraction peaks at 11.9°, 23.8°, 34.7°, 39.3°, 46.9°, 59.9° and 61.5° match well with the (006), (0012), (204), (2010), (2016), (220) and (2120) planes of NiFe-LDH ($Ni_6Fe_2(CO_3)(OH)_{16}·4H_2O$, PDF#26-1286), demonstrating the successful formation of NiFe-LDH phase. Meanwhile, energy-dispersive X-ray spectroscopy (EDS) mappings show a uniform distribution of Ni and Fe on the nanosheets with a Ni/Fe ratio of 2.38 (Fig. S2 in Supporting information).

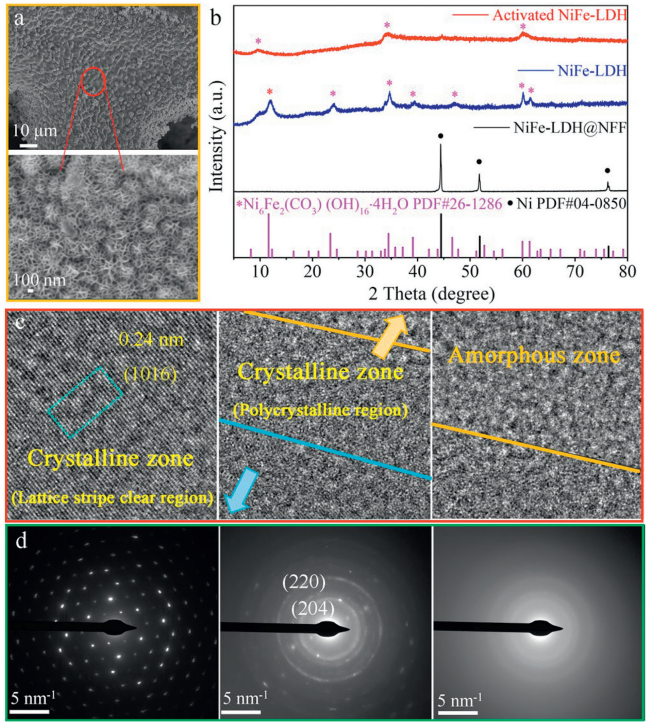

Fig. 2. Characterizations of NiFe-LDH@NFF. (a) SEM images, (b) XRD patterns of NiFe-LDH@NFF, NiFe-LDH powder, and activated NiFe-LDH powder. (c) TEM images and (d) SAED patterns.

Interestingly, the methanol-mediated corrosion engineering yielded a high-entropy NiFe-LDH@NFF material with rich composition of constituent phases [26]. From the high-resolution TEM image (Fig. 2c and Fig. S3 in Supporting information), the compartmentation of three different phases can be clearly seen. The highly crystalline region displayed obvious lattice stripes with distinct lattice fringes of 0.25 nm, matching well with the (1016) facet of NiFe-LDH. Adjacent to it, polycrystalline regions with blurred and discontinuous lattice stripes are clearly visible. Proximate to the transitional polycrystalline region, distant from the well-defined

large single-crystalline zone, amorphous region with no detectable lattice fringes can be discerned. Therefore, the microstructure of the as grown NiFe-LDH is at a composite state that includes monocrystalline, polycrystalline and amorphous phases, which is in line with the three distinct selected area electron diffraction (SAED) patterns (Fig. 2d) displaying bright dots, randomly dotted rings, and diffused thick rings, respectively. The obviously chaotic phase and irregular structure within the single elemental composition gives rise to abundant boundaries and vacancies for facile atomic constraining and electronic rearrangements making them more adaptive before equilibrium is reached [27,28].

To investigate the possible formation and reveal the role of NH_4F, Fe@CC and NH_4F-Fe@CC were prepared on carbon cloth (CC). Even only with $Fe(NO_3)_3$ and methanol, the microscopic morphology of Fe@CC still maintains the nanosheet array structure (Fig. S4a in Supporting information). The XRD pattern of Fe@CC reveals a distinct diffraction peak located at about 10°, which agrees well with the reported iron alkoxide (Fig. S4d in Supporting information) [29-31]. The Lewis acid centers of Fe^{3+} coordinate the conjugate base of methanol leading to its deprotonation [31]. The dilute and uniform vapor state of methanol allows for its dispersed bonding with iron cations, which greatly simplifies the nanosheet formation. We further explored the effect of NH_4F. Although the nanosheet of NH_4F-Fe@CC is smaller and denser, the microscopic morphology remains the same (Fig. S4b in Supporting information). The XRD pattern of NH_4F-Fe@CC shows a weaker and wider peak around 10° (enlarged Fig. S4d), confirming that the presence of NH_4F reduces the crystallinity and promotes the denser nanosheet array. Even after calcination (Fig. S4c in Supporting information), the microstructure does not show significant changes, confirming its mechanical stability. The XRD patterns of NH_4F-Fe@CC-400 (Fig. S4d) and Fe@CC-400 (Fig. S5 in Supporting information) can be well indexed to Fe_2O_3 (JCPDS No. 03-0800), verifying the existence of coordinated iron salt intermediates [32].

As for NFF, the reaction process becomes more complex [33]. A reasonable formation process of NiFe-LDH@NFF is illustrated in Fig. 1b. Due to the strong oxidizing ability of Fe^{3+}, bare metals including Ni and Fe can be oxidized to metal cations [20,34]. The F^- ions likewise promote this corrosion process [35]. The sparse water liberated from $Fe(NO_3)_3{\cdot}9H_2O$ likely becomes highly dispersed and surrounded by copious methanol molecules. Naturally, the overall environment containing Ni^{2+}, Fe^{2+}, Fe^{3+}, and NH_4F gives rise to limited hydroxide source for constructing the LDH host layers. The uneven water vapor atmosphere and scare source of OH^-, originating from the pyrolysis of NH_4F and redissolution of NH_3, ultimately lead to the high-entropy NiFe LDH structure. During this reaction process, carbon dioxide (CO_2) from the air atmosphere is also an important driving factor for the fabrication of interlayer CO_3^{2-} anions. These unique synthesis conditions did not yield conventional NiFe-LDH with good crystalline properties, but a high-entropy structure containing spatially gradient crystallinity having distinct crystalline and amorphous phases interconnected by polycrystalline regions. Our previous work has pointed out that abundant methanol molecules can directly lead to crystalline-amorphous heterophase structure [36]. The F^- ions in the methanol vapor could reduce the LDH crystallinity. Meanwhile, the presence of NH_4^+ in the reaction system is conducive to promote LDH formation. Thus, the chaotic distribution of phases is attributed to the kinetic effects of methanol vapor molecules (dispersive factor), F^- ions (destructive factor), and NH_4^+ ions (promoting factor).

To evaluate the high-entropy NiFe LDH@NFF samples, we performed electrochemical measurements without IR compensation. Along with the continuous cyclic voltammetry (CV) scanning (Fig. 3a), the redox process of Ni^{2+}/Ni^{3+} exhibited obvious variations including peak current and position [37,38]. More specifically, the oxidation peak current increased while the peak potential progressively moved to a lower position. Here, the catalyst−electrolyte interface underwent dynamic changes related to chemical composition and valence states [39]. The shift in the oxidation peak can be attributed to the fluctuation of nickel-iron ratios and the related structural transformation. Dissolution and redeposition of iron allow self-repair of the NiFe-based electrodes [16]. As gained from EDS (Figs. S2 and S6 in Supporting information), the CV scanning indeed increased NiFe ratio of the NiFe-LDH@NFF from the pristine 2.38 to the activated 2.61 after 100^{th} cycles, consisted with the trend obtained by ICP-MS (Table S1 in Supporting information). Meantime, the metal elements are still uniformly distributed in the nanosheets. In agreement with the relevant literature, moving to a lower voltage represents a gradual decrease of iron ratio [38]. On the other hand, the peak current is related to the concentration of effective Ni^{2+} [40]. The electrochemical active surface area (ECSA) was estimated based on the double-layer capacitances (C_{dl}) (Figs. S7a and b in Supporting information, Fig. 3b). The activated NiFe-LDH has a C_{dl} value of 2.22 mF/cm^2, much larger than that of 2.01 mF/cm^2 for the sample after the 10^{th} CV cycle. The higher C_{dl} value demonstrates that the activated NiFe-LDH can provide more accessible catalytic sites, providing a supplemental explanation to the shift and enhancement of the oxidation peaks.

The linear sweep voltammetry (LSV) was carried out to better understand the activation process (Fig. S7c in Supporting information). The 10^{th} catalyst has a poor OER activity showing an overpotential of 264 mV at 10 mA/cm^2. By contrast, after 100 CV cycles, this overpotential value decreased to 249 mV confirming the *in-situ* activation process. Notably, when the overpotential is low, a smaller Tafel slope of 51.7 mV/dec is obtained for the activated NiFe-LDH@NFF compared to that of 53.5 mV/dec after the 10th (Fig. 3c). Therefore, continuous CV enhanced the intrinsic activity of the activated NiFe-LDH, rendering it excellent OER performance, outperforming that of commercial IrO_2 (Figs. S7d-f in Supporting information). Correspondingly, the Nyquist plots show that the activated NiFe-LDH@NFF displays a lower charge transfer resistance, indicating that the activation process can markedly facilitate charge transfer (Fig. 3d). Thanks to the atomic substrate-LDH bonding arising from the semi-sacrificial metal support, the activated catalyst shows favorable operating stability, providing a stable 1 A/cm^2 current density for a period of more than 120 h (Fig. 3e). After the high-current stability test, the TEM image and the corresponding SAED pattern of the nanosheet confirm the coexistence of amorphous and polycrystalline phases (Fig. S8 in Supporting information). This is also verified by the XRD pattern of the activated electrode showing broad hump indicating amorphous phases (Fig. 2b). The high-entropy crystalline-amorphous structure is highly adaptable to the localized acidic environment formed under high currents.

For practical application, we further tested the OER performance in 6 mol/L KOH solution. Similar *in-situ* electrochemical activation took place, exhibiting progressively higher current values with negligible positional shift (Fig. 3f). Here, the double-layer capacitance measurements confirmed the increase of ECSA from 1.95 mF/cm^2 to 2.59 mF/cm^2 (Fig. S9a in Supporting information and Fig. 3g). Considering the higher 6 mol/L KOH solution, the metal ion dissolution from the surface could be much faster than in 1 mol/L KOH solution. The absence of positional shift can demonstrate that the dissolution and reincorporation of metal ions have reached a *quasi*-equilibrium. The corresponding LSV curves also confirm this trend (Fig. S9b in Supporting information). Furthermore, the higher activity of the activated NiFe-LDH@NFF is reflected by its smaller charge transfer resistance (Fig. S9c in Supporting information) as well as the lower Tafel slope (44.8 mV/dec) (Fig. S9d in Supporting information). Given the above demonstrated high-current stability, the testing was conducted in the

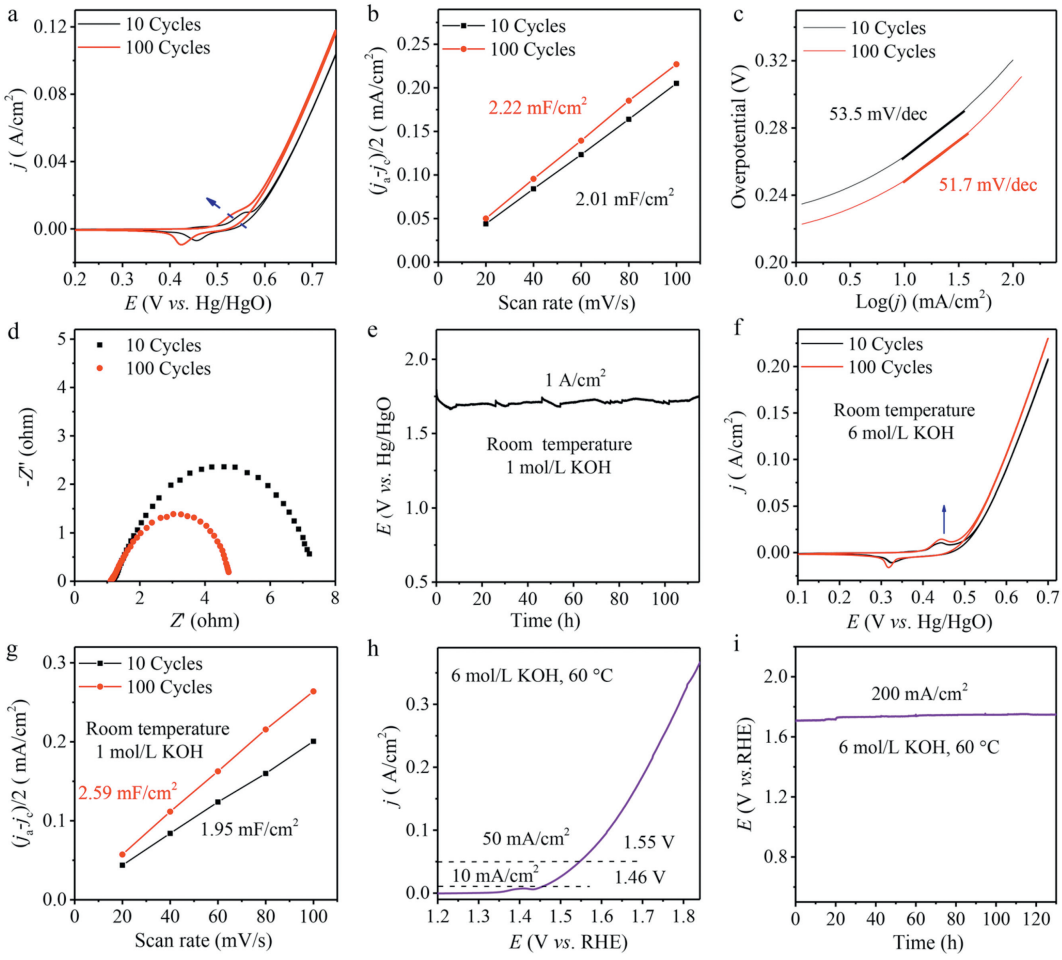

Fig. 3. NiFe-LDH@NFF electrocatalytic measurements. (a) CV curves, (b) C_{dl} measurements, (c) Nyquist plots, (d) Tafel slopes, (e) durability tests at 1 A/cm^2, (f) CV curves in 6 mol/L KOH solution, (g) C_{dl} measurements in 6 mol/L KOH solution, (h) LSV curve of the two-electrode configuration and (i) corresponding durability test result.

harsher industrial operating condition (60 °C, 200 mA/cm^2). Under the two-electrode system (Fig. 3h), the activated NiFe-LDH@NFF afforded current densities of 10 and 50 mA/cm^2 at 1.46 V and 1.55 V, respectively. There was only less than 10 % potential increase while holding the high current density of 200 mA/cm^2 for at least 130 h (Fig. 3i). Compared to recently reported OER catalysts with high-entropy structures, activated NiFe-LDH@NFF presents the significant stability advantage (Table S2 in Supporting information). Overall, the excellent stability can be attributed to the semi-sacrificial support and the irregular crystalline phase, which makes it less likely to form localized acidic environments and allows OH^- to diffuse more easily.

The electrochemical activation induces subtle adaptive atomic arrangement while the overall microstructure is still within the frame of high-entropy crystalline-amorphous heterophase [41]. X-ray photoelectron spectroscopy (XPS) was employed to further explore the surface chemistry and oxidation state (Fig. S10 in Supporting information). As can be observed in Fig. 4a, two spin–orbit doublets of Ni $2p_{3/2}$ (855.4 eV), Ni $2p_{1/2}$ (872.9 eV) and satellites (860.8 and 879.8 eV, abbreviated as "sat.") can be indexed to Ni^{2+}, while another pair of peaks (856.6 and 874.8 eV) and satellites (862.8 and 881.5 eV) are assigned to Ni^{3+}. Specifically, the Ni $2p_{3/2}$ peak of activated NiFe (oxy)hydroxides obviously shifts to higher binding energy, suggesting that partial electrons are transferred. The ratio of Ni(III)/Ni(II) for activated NiFe-LDH is estimated to be 1.67, larger than that of 0.56 for the pristine NiFe-LDH [42]. The peaks located at 706.6 eV is assigned to metallic Fe. The two peaks with binding energies at about 709 eV and 711 eV correspond to Fe^{2+} and Fe^{3+}, respectively. Similarly, the ratio of Fe^{3+} $2p_{3/2}$/Fe^{2+} $2p_{3/2}$ decreases from 2.27 to 1.65 (Fig. 4b), which manifests the efficient electron transfer from Ni to Fe during activation. For the fresh NiFe-LDH@NFF (Fig. 4c), the Raman spectra show three representative bands at 525 cm^{-1}, 702 cm^{-1} and 1057 cm^{-1}, which are assigned to Ni^{II}–OH, Ni^{II}O–H, and the C–O stretching modes of interlayer carbonate anions, respectively [43]. Signals of surface structure rearrangement become clear after CV cycles (Fig. S11 in Supporting information). The emergence of new Raman bands at 474 and 554 cm^{-1} suggests the formation of NiOOH phase [44]. These two vibrations are ascribed to the Eg Ni^{III}–O bending vibration mode and A1g Ni^{III}–O stretching vibration [45]. The characteristic peaks of Fe^{3+} species were likely masked by the intense Ni–O and Ni–OH peaks, consistent with other literature reports [46]. The facile surface structure rearrangement, eased by the high-entropy structure, facilitate anodic oxidation to the beneficial NiOOH active sites.

To further probe the origin of high catalytic activity and stability, electrochemical quartz microbalance with dissipation monitoring (EQCM-D) method was chosen to track the sorption-desorption behavior [47]. After injection of 1 mol/L KOH solution (Fig. S12 in Supporting information), the ΔD and Δf/n values became almost unchanged within 5000 s. As indicated in CV curves, the increasing current intensity reflects an obviously enhanced OER performance (Fig. S13a in Supporting information, Fig. 4d). Along with the periodic sorption−desorption changes, the time profile of Sauerbrey

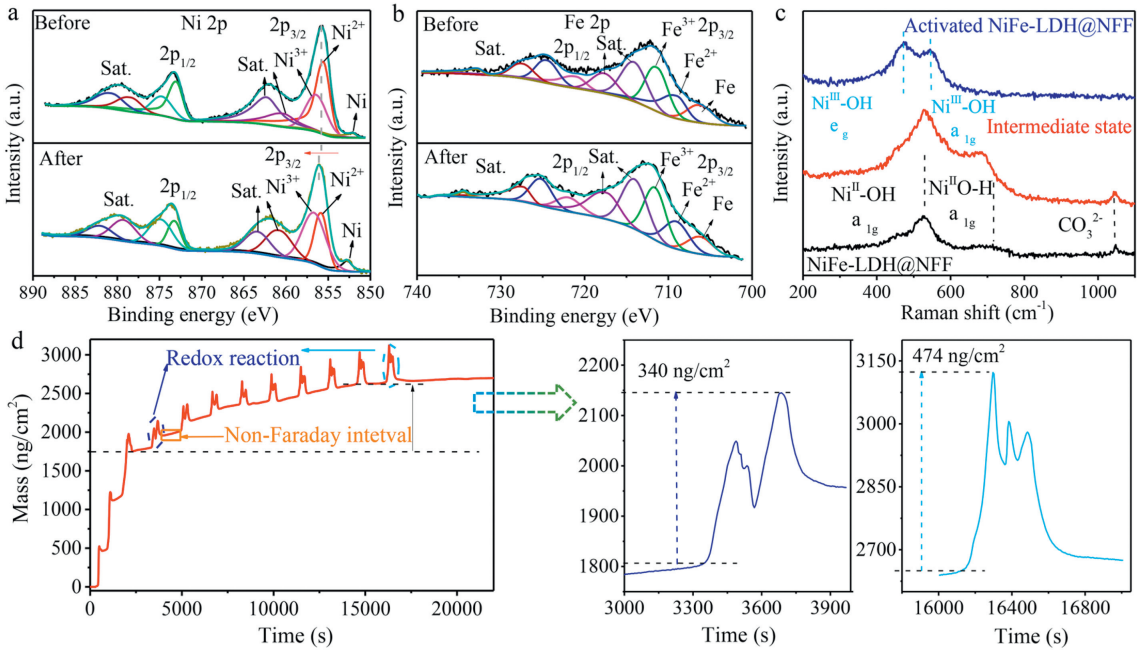

Fig. 4. Surface characterizations of NiFe-LDH@NFF. (a) Ni 2p XPS spectra before and after activation process, (b) corresponding Fe 2p XPS spectra, (c) Raman spectra and (d) mass *vs.* time showing the periodic fluctuations during the CV cycles.

mass indicates an overall gradually increasing trend. The weight gain in the non-Faraday interval could mean electrochemical modification of the active sites adsorbing more water molecules and hydroxyl ions giving rise to oxyhydroxide. Within a single redox cycle, the peak height, that is the Sauerbrey mass between the highest adsorption point and the lowest one, is also getting larger from 360 ng/cm^2 to 474 ng/cm^2. Meantime, $\Delta D/n$ also displays an increasing trend (Fig. S13b in Supporting information), suggesting that the surface became softer. The real-time information from this surface-sensitive technique quantitively reveals the activation process, which gradually optimizes the structure and arrangement of active sites. In light of these findings, the mixed crystalline states within single composition likely contribute to the facile electrochemical activation that affords more active and readily accessible catalytic sites with softer structure.

In summary, a facile corrosion engineering route was explored to fabricate high-entropy NiFe-LDH on semi-sacrificial NFF under methanol steam atmosphere. The co-presence of single crystalline, polycrystalline, and amorphous phases within one composition mainly results from the synergistic *quasi*-equilibrium of ammonium fluoride and methanol vapors. The as-prepared FeNi-LDH@NFF could be further activated gradually to a remarkable height during OER, accompanied with an outstanding stability at 1 A/cm^2. XPS spectra, *operando* Raman, and EQCM-Q systematically confirmed the surface transformation processes. Under industrial conditions (6 mol/L KOH, 60 °C), NiFe-LDH@NFF can achieve an output current density of 10 mA/cm^2 at the cell voltage of 1.46 V, and 50 mA/cm^2 at 1.55 V. Furthermore, the controlled corrosion engineering strategy enhances the operating stability in the 6 mol/L KOH electrolyte. This work provides a simple one-step approach to fabricate low-cost durable electrocatalysts for industrial applications.

Declaration of competing interest

The authors declare that they have no known competing financial interests or personal relationships that could have appeared to influence the work reported in this paper.

CRediT authorship contribution statement

Jinqiang Gao: Writing – original draft, Investigation, Conceptualization. **Haifeng Yuan:** Validation, Formal analysis. **Xinjuan Du:** Data curation. **Feng Dong:** Data curation. **Yu Zhou:** Methodology, Formal analysis. **Shengnan Na:** Methodology, Formal analysis. **Yanpeng Chen:** Methodology. **Mingyu Hu:** Funding acquisition, Data curation. **Mei Hong:** Writing – review & editing, Supervision, Project administration, Methodology, Funding acquisition. **Shihe Yang:** Writing – review & editing, Project administration, Funding acquisition.

Acknowledgments

This work was supported by the Guangdong Science and Technology Program (No. 2023A0505010018), the National Natural Science Foundation of China (No. 22309155), and the Shenzhen Science and Technology Program (No. JCYJ20200109140421071).

Supplementary materials

Supplementary material associated with this article can be found, in the online version, at doi:10.1016/j.cclet.2024.110232.

References

[1] R. Peters, J. Berlekamp, C. Kabiri, et al., Nat. Rev. Earth Environ. 5 (2024) 137–151.
[2] R. Fan, C. Liu, Z. Li, et al., Nat. Sustain. 7 (2024) 158–167.
[3] P.F. Guo, Y. Yang, B. Zhu, et al., Carbon Energy 6 (2024) e532.
[4] F. Osselin, C. Soulaine, C. Fauguerolles, et al., Nat. Geosci. 15 (2022) 765–769.
[5] Z. Gu, J. Le, H. Wei, et al., Chin. Chem. Lett. 35 (2024) 108849.
[6] Q. Li, Q. Zhang, W. Xu, et al., Adv. Energy Mater. 13 (2023) 2203955.
[7] S.Z. Oener, A. Bergmann, B.R. Cuenya, Nat. Synth. 2 (2023) 817–827.
[8] X. Yu, Z. Pan, C. Pei, et al., Chin. Chem. Lett. 35 (2024) 108484.
[9] L. Magnier, G. Cossard, V. Martin, et al., Nat. Mater. 23 (2024) 252–261.
[10] J. Wang, Y. Gao, H. Kong, et al., Chem. Soc. Rev. 49 (2020) 9154–9196.
[11] J. Mei, Y. Deng, X. Cheng, et al., Chin. Chem. Lett. 35 (2024) 108900.
[12] G.H. Gao, R.Z. Zhao, Y.J. Wang, et al., Chin. Chem. Lett. 35 (2024) 109181.
[13] L. Lv, Z. Yang, K. Chen, et al., Adv. Energy Mater. 9 (2019) 1803358.
[14] Y. Yang, Q.N. Yang, Y.B. Yang, et al., ACS Catal. 13 (2023) 2771–2779.
[15] Y. Jiang, Y. Li, Y. Jiang, et al., Chin. Chem. Lett. 33 (2022) 4003–4007.
[16] Q. Zhang, W. Xiao, H.C. Fu, et al., ACS Catal. 13 (2023) 14975–14986.

[17] R. Chen, S.F. Hung, D. Zhou, et al., Adv. Mater. 31 (2019) 1903909.
[18] X. Lei, Q. Tang, Y. Zheng, et al., Nat. Sustain. 6 (2023) 816–826.
[19] Y. Liu, X. Liang, L. Gu, et al., Nat. Commun. 9 (2018) 2609.
[20] Y. Li, Y. Wu, M. Yuan, et al., Appl. Catal. B: Environ. Energy 318 (2022) 121825.
[21] Q. Jia, J.Q. Gao, C. Qiu, et al., Chem. Eng. J. 433 (2022) 134552.
[22] F. Dong, H. Duan, Z. Lin, et al., Appl. Catal. B: Environ. Energy 340 (2024) 123242.
[23] Y. Yang, L. Dang, M.J. Shearer, et al., Adv. Energy Mater. 8 (2018) 1703189.
[24] Y.F. Song, Z.Y. Zhang, H. Tian, et al., Chem. Eur. J. 29 (2023) e202301124.
[25] Q. Kang, D. Lai, W. Tang, et al., Chem. Sci. 12 (2021) 3818–3835.
[26] S. Schweidler, M. Botros, F. Strauss, et al., Nat. Rev. Mater. 9 (2024) 266–281.
[27] G. Wan, J.W. Freeland, J. Kloppenburg, et al., Sci. Adv. 7 (2021) eabc7323.
[28] D. Li, Y. Qin, J. Liu, et al., Adv. Funct. Mater. 32 (2021) 2107056.
[29] X. Xu, J. Luo, S. Wei, et al., Chem. Eng. J. 398 (2020) 125649.
[30] P. Liu, J. Liu, J. Liu, et al., J. Alloys Compd. 769 (2018) 873–880.
[31] J. Lee, H. Lee, B. Lim, J. Ind. Eng. Chem. 58 (2018) 100–104.
[32] X. Li, B. Zhang, C. Ju, et al., J. Phys. Chem. C 115 (2011) 12350–12357.
[33] W. Zhao, H. Xu, H. Luan, et al., Adv. Energy Mater. 12 (2021) 2102372.
[34] S. Du, Z. Ren, X. Wang, et al., ACS Nano 16 (2022) 7794–7803.
[35] N. Yamada, S. Kitano, Y. Yato, et al., ACS Appl. Energy Mater. 3 (2020) 12316–12326.
[36] J. Gao, C. Qiu, M. Ju, et al., Appl. Catal. B: Environ. Energy 323 (2023) 122165.
[37] M.B. Stevens, L.J. Enman, A.S. Batchellor, et al., Chem. Mater. 29 (2016) 120–140.
[38] L. Trotochaud, S.L. Young, J.K. Ranney, et al., J. Am. Chem. Soc. 136 (2014) 6744–6753.
[39] L. Liu, A. Corma, Nat. Rev. Chem. 5 (2021) 256–276.
[40] N. Elgrishi, K.J. Rountree, B.D. McCarthy, et al., J. Chem. Educ. 95 (2017) 197–206.
[41] S. Shen, Z. Wang, Z. Lin, et al., Adv. Mater. 34 (2022) 2110631.
[42] M. Görlin, J. Halldin Stenlid, S. Koroidov, et al., Nat. Commun. 11 (2020) 6181.
[43] L. Peng, N. Yang, Y. Yang, et al., Angew. Chem. Int. Ed. 60 (2021) 24612–24619.
[44] Z. Zhou, Y.N. Xie, L. Sun, et al., Appl. Catal. B: Environ. Energy 305 (2022) 121072.
[45] M.W. Louie, A.T. Bell, J. Am. Chem. Soc. 135 (2013) 12329–12337.
[46] L. Gao, X. Cui, Z. Wang, et al., Proc. Natl. Acad. Sci. U. S. A. 118 (2021) e2023421118.
[47] M. Ju, R. Cai, J. Ren, et al., ACS Appl. Mater. Interfaces 13 (2021) 37063–37070.